Superconductor
Science and
Technology

ACCEPTED MANUSCRIPT • OPEN ACCESS

Vortex dynamics study on an uniaxially textured YBCO/MgO superconducting film from magnetic measurements

To cite this article before publication: H. Sanchez Cornejo *et al* 2025 *Supercond. Sci. Technol.* in press https://doi.org/10.1088/1361-6668/adb6d8

Vortex dynamics study on an uniaxially textured YBCO/MgO superconducting film from magnetic measurements

H. Sanchez Cornejo[a(*)], A. Bustamante Domínguez[a], S.N. Holmes[b], J.W. Seo[c], J. Albino Aguiar[d], V.A.J. Silva[d], C.H.W. Barnes[e], L. De Los Santos Valladares[d,e,(*)]

[a] Laboratorio de Cerámicos y Nanomateriales, Facultad de Ciencias Físicas, Universidad Nacional Mayor de San Marcos, Ap. Postal 14-0149, Lima 14, Perú.

[b] Department of Electronic and Electrical Engineering, University College London, Torrington Place, London WC1E 7JE, UK.

[c] College of Science and Technology, Yonsei University, 1 Yonseidae-gil, Wonju, Gangwon-do, 26493, South Korea.

[d] Programa de Pós-Graduação em Ciências de Materiais, Centro de Ciências Exatas e da Natureza, Universidade Federal de Pernambuco, 50670-901 Recife-PE, Brazil.

[e] Cavendish Laboratory, Department of Physics, University of Cambridge, J. J. Thomson Ave., Cambridge CB3 0HE, United Kingdom

(*) Corresponding authors emails: henrysanchez45@gmail.com (H. Sanchez Cornejo) and ld301@cam.ac.uk (L. De Los Santos Valladares)

ABSTRACT

The vortex dynamics of an undoped uniaxially textured $YBa_2Cu_3O_{7-\delta}$ (YBCO) superconducting film grown onto a MgO (100) substrate was inspected by applying the vortex glass and collective-pinning models. The texture and structural characterization studied by XRD revealed a uniaxially (00l) YBCO layer, which coexists with minor Y_2BaCuO_5 and CuO phases. The temperature dependence of the magnetization in the superconducting state reveals a critical temperature T_C = 88 K. By measuring the hysteresis loops ($M(H)$) at 10 - 70 K, the critical fields H_{C1}, H_{C2}, H_P and H_{irr} were estimated and a vortex matter diagram is sketched. By using the Bean model, the critical current density values $J_C(T,H)$ are obtained and the typical peak effect is observed. The vortex dynamics mechanism is discussed taking into account four vortex feature regimes in the double-logarithmical $J_C(H)$ curves. The vortex pinning mechanism is discussed by obtaining the pining force, F_P, its normalization, $f(h)$, and magnetic relaxation $M(t)$ measurements taken in field cooling (FC) mode at 10 – 60 K. The glassy exponent μ and the characteristic energy $U(J,T)$ in the vortex glass model were estimated following the Maley method. The collective-pinning model is used to discuss the possible vortex regimes mechanism (individual flux lines, small bundles and large bundles of pinned flux). Eventually, the $E(J)$ curves, expressed from the swept field and creep measurements, show a power-law behaviour, in agreement with the vortex matter.

Keywords: Vortex dynamics; YBCO superconductor; Uniaxial thin film; Magnetic properties of YBCO.

1.- INTRODUCTION

$YBa_2Cu_3O_{7-\delta}$ (YBCO) is one of the most studied high-temperature superconducting (HTSC) material [1-3]. High-quality YBCO textured films have been developed in recent years in order to understand the superconducting phenomena and to apply them in electrical devices [4]. Because YBCO possesses a strong magnetic anisotropy [5], several studies have been focused on biaxially textured YBCO films [4, 6, 7] in order to improve the J_C values by ordering the CuO_2 superconducting planes [5]. However, the critical current density is influenced by the strength of the vortex pinning in the material. Thus, in order to apply industrially YBCO, it is important to understand the vortex pinning mechanism in partially textured layers and under many different conditions.

In the other hand, vortex physics strongly governs the physical properties of superconductors [8]. The state-of-the-art about this topic is performed in the study of vortex matter by simulations and theorical models [9-11]. Few recent experimental works have focused on transport measurements, with the disadvantage that the heating dissipation on the contacts limits the experimental analysis [12]. Among the theoretical models, the Anderson-Kim or flux-creep [13], Giant flux creep [14], Zeldov logarithmic barrier [15], Vortex-glass [16] and FGVL [17] fit well the experimental data. Whereas, the Gingzburg - Landau framework theory, the Ovchinikov and Ivlev equations [18], and the Van der Beek model [19] describe the field dependence of J_C behavior in YBCO and other HTSC materials.

Irregularities in the superconducting film can disrupt translational symmetry and thus can pin vortices. They are usually in the 2ξ (ξ, coherence length) dimension, with $\xi_{ab}(0\ \mathrm{K}) \approx 2\ \mathrm{nm}$ for YBCO [20]. Thus, understanding the vortex matter under different experimental conditions, including vortex-vortex and vortex-pinning center interactions, provides a pathway for improving the performance of well-textured YBCO films. In fact, a detailed knowledge of the flux pinning due to naturally occurring defects of YBCO allows a clear vision for the enhancement of J_C by introducing additional artificial pinning centres (APCs) into the superconducting matrix [21-23].

The existing studies on vortex dynamics in YBCO have been focused in bulk and in bi-axial thin films, with special interest in the improvement of the transport capabilities by both, ordering the CuO_2 superconducting planes and (or) inserting APCs [21-25]. In the present work, the vortex dynamics in the presence of natural pinning centres (e.g. secondary phases, stacking faults, grain boundaries, misoriented grains, point defects) is studied in an undoped uniaxial YBCO superconducting film. Also, in the present work, both, the vortex glass and the collective-pinning models are tested to determine which one fits best the experimental data. In this way, the study is carried out at different experimental conditions, such as different ranges of temperature and under different applied magnetic fields in order to obtain a wide landscape of the pinning matter as from intrinsic pinning mechanisms in the film. Moreover, since the data presented in this work has been obtained under several experimental conditions, and rigorously analysed by the models mentioned above, the present results provide valuable examples on how to apply the theory of vortex dynamics in superconducting films.

2.- EXPERIMENTAL

A uniaxial YBCO film was purchased from the CERACO Ceramic Coating GmBH Inc. Germany, which was deposited on an (100) high textured MgO substrate by Sputtering technique. This sample is sold by CERACO suggesting application on low temperature electronics, multilayers and submicron structures. Additional information about the characterization of the sample as well as its magnetic properties is found in reference [5]. The crystallization of the sample was studied by X-ray diffraction (XRD). The data were collected from 8º to 80º (0.01º step) using a powder universal diffractometer Bruker D8 FOCUS with Cu

$K_{\alpha 1}$ radiation (λ = 1.54056 Å). The crystallite size was estimated from the basic Scherrer's formula, neglecting peak broadening caused by residual stresses in the films [26].

$$D = \frac{K\lambda}{\beta_{hkl}\cos\theta_{hkl}} \quad (1)$$

Here D is the average crystallite size, λ is the wavelength of the applied X-ray ($\lambda_{\text{Cu-K}\alpha 1}$ = 0.154056 nm), θ_{hkl} is the Bragg's angle, β_{hkl} is the width of the x-ray peak on the 2θ axis, which were easily found by measuring the full width at the half maximum (FWHM) of the reflection and K is the so-called Scherrer Constant. K depends of the crystallite shape and the size distribution, indices of the diffraction line, and the actual definition used for β whether FWHM or integral breadth [27]. K can have values anywhere from 0.62 and 2.08. In this paper, K = 0.916 was used. Further, microstrain in the crystallite or nanocrystal also affects the width β, which needs to be considered in an accurate analysis. Spatial fluctuations in the alloy composition can also affect the width. Therefore, the calculated values of D represent estimates but enough for the purpose of the work.

The magnetization hysteresis loops were measured using a Quantum Design DC-MPMS-SQUID magnetometer equipped with a 7 T superconducting magnet. All the $M(H)$ measurements were done in a field range 0 – 5.5 T, with the applied magnetic field perpendicular to the surface sample, and at different temperatures T = 10 – 70 K. The superconducting transition temperature T_C was determined from temperature-dependent measurements of the magnetization under H_{ext} = 500, 1000, 5000 and 10000 Oe. Temperature-dependent measurements under several H_{ext} applied both transversal and along to the film were previously reported and the T_{C} variation studied [5].

Magnetic relaxation measurements were also performed with the DC-MPMS-SQUID magnetometer. The sample was field-cooled at T = 10, 30, 40 and 60 K under 1 T applied magnetic field, parallel to the *c*-axis. The H_{ext} was then suppressed and the decay of the magnetization was measured with time. The scan length of the magnetometer was reduced to 30 mm in order to minimize the effects of field inhomogeneities. The ramped up and down for the field were for both cases equal to 500 Oe/sec.

The critical current density J_{C} values were estimated using the critical state Bean model between $H_{\text{P}} < H < H_{\text{irr}}$, following the expression 2, valid for a rectangular sample [28]:

$$J_C = \left[\frac{20\Delta M}{w\left(1-\frac{w}{3l}\right)}\right] \quad (2)$$

Where M^+ and M^- are the magnetization branches in the fully penetrated state for decreasing and increasing applied fields, respectively. Here $\Delta M = M^- - M^+$, the unit of ΔM is emu/cm^3, and w, l are the width and length of the sample measured in cm ($w < l$), respectively. For the different magnetization measurements, a square-shape YBCO film with dimensions $w = l = 4$ mm and t =1 μm was used. Here, t is the thickness of the undoped film.

3.- RESULTS AND DISCUSSION

3.1.- *Magnetic phase diagram*

The applied magnetic field dependence of the magnetization loops, $M(H)$, measured at T = 10, 20, 30, 40, 50, 60 and 70 K, shown in Fig. 1(a), reveal hysteresis. The demagnetization factor was properly accounted

in the used geometry for all loops. Since the magnetization values decay rapidly as the temperature is increased, the hysteresis loops are shown in arbitrary units for eye-guide. The figure S1 in the Supporting Information shows the $M(H)$ loops in emu/cm^3 units. In order to study the vortex matter, the superconducting critical fields H_{c1}, H_{c2} and H_{irr} were identified from both, the $M(H)$ and the $M(T)$ curves. The irreversible line, that correspond to first-order transition on the vortex lattice, has an experimental behaviour defined as [20, 30]:

$$H_{irr} = H_{irr}(0)\left(1 - \frac{T}{T_C}\right)^n \tag{3}$$

which describes the experimental data in the field range from 0 up to 25 T ($n = 1.4$), while for $n = 1.5$ the expression corresponds to the case of thermally activated flux creep. Nonetheless, at $n = 1.3$, the line limits the transition from vortex glass to vortex liquid [20]. Table 1 summarizes the experimental $H_{\mathrm{irr}}(T)$ values obtained from the hysteresis loops, in which each irreversible field value is estimate from the point where M_{irr} becomes zero.

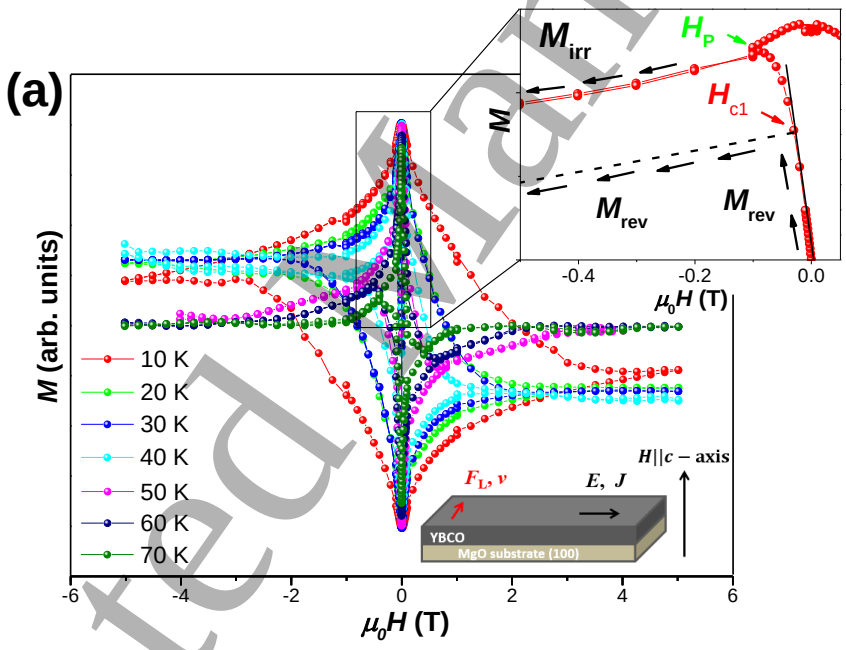

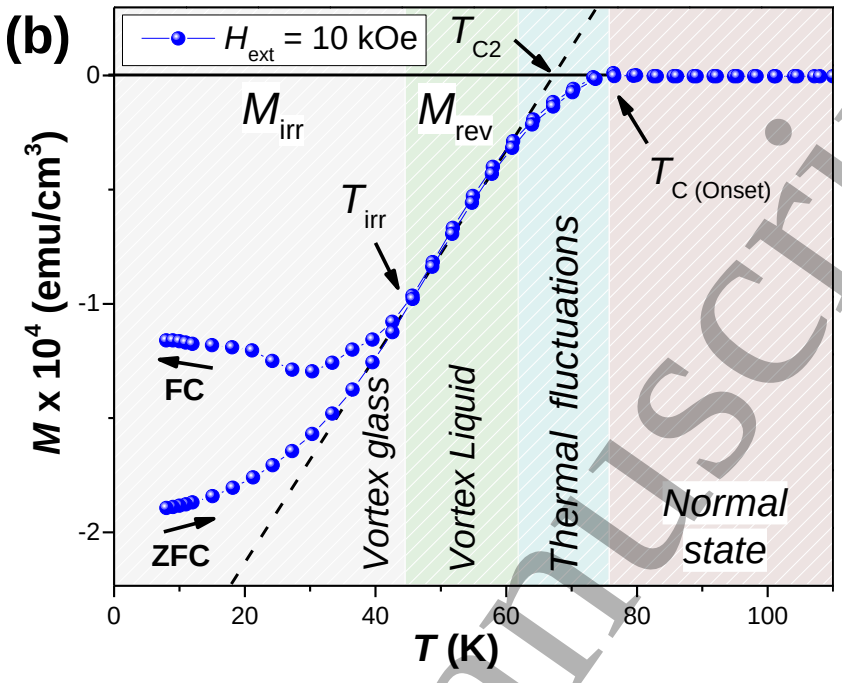

Fig 1. a) $M(H)$ loops of a YBCO/MgO film measured under $H_{ext} \parallel c$-axis at T = 10 – 70 K, showing hysteresis. Inset: $M(H)$ at 10 K zoomed around the initial cycle in order to observe the reversible magnetization and the arising of the irreversible magnetization. b) Temperature-dependence of the magnetization at H_{ext} = 10 kOe. The different superconducting stages are showed.

The irreversible field values, experimentally obtained from the $M(H)$ curves, were plotted against the temperature and the loop was fitted using equation (3). In this way, $n \approx 1.3$ is obtained (see Fig. S2(a)). This means that the first-order irreversible line of the sample corresponds a glass-liquid vortex transition. Once the expression for the irreversible line is obtained, the different T_{irr} values from the $M(T)$ curves allow computing the corresponding $H_{irr}(T_{irr})$ values.

On the other hand, the lower critical field $H_{C1}(T)$ is estimated from the point where the linear field-dependence of magnetization disappears (or where the M_{irr} appear due to the magnetic flux penetration on the material) in Fig. 1(a). Therefore, for each T, the point in which the field deviates from the initial linear dependence, corresponds to $H_{C1}(T)$. This initial linear behaviour of the magnetization corresponds to the Meissner state response (perfect diamagnetism). Considering an applied field $H > H_{C1}$, the magnetic field starts to penetrate the sample but exists a region between $H_{C1} < H < H_P$ in which the magnetic flux does not reach the centre of the sample and thus, it is not possible to apply the critical state model. Here, H_P corresponds to the penetration field which guarantees that the field reaches the centre of the film.

Similarly, the second critical field $H_{C2}(T)$ values are determined from both $M(H)$ and $M(T)$ experimental curves by finding the field value in which M_{rev} drops to zero. From $M(H)$ loops, the corresponding $H_{C2}(T)$ value is determined by extrapolating the M_{rev} curve to zero. Besides, the $M(T)$ curves present a linear dependence at T_{irr} (reversible behavior, M_{rev}) except at temperatures near T_C, in which thermal fluctuations dominate the system (see Fig. 1(b), in which the different superconducting stages are highlighted). Therefore, by extrapolating the linear part of M_{rev} to $M = 0$ in the $M(T)$ loop, the $H_{C2}(T_{C2})$ can be also estimated. Considering this, the Fig. 2 shows the temperature-dependence of the magnetization measured

at H_{ext} = 500, 1000, 5000 and 10 000 Oe applied along the c-axis. Once the $H_{C2}(T)$ values are experimentally obtained, the resulting curve can be fitted by the following expression [20] (see Fig. S2(b)):

$$H_{C2} = H_{C2}(0)\left(1 - \frac{T}{T_C}\right) \quad (4)$$

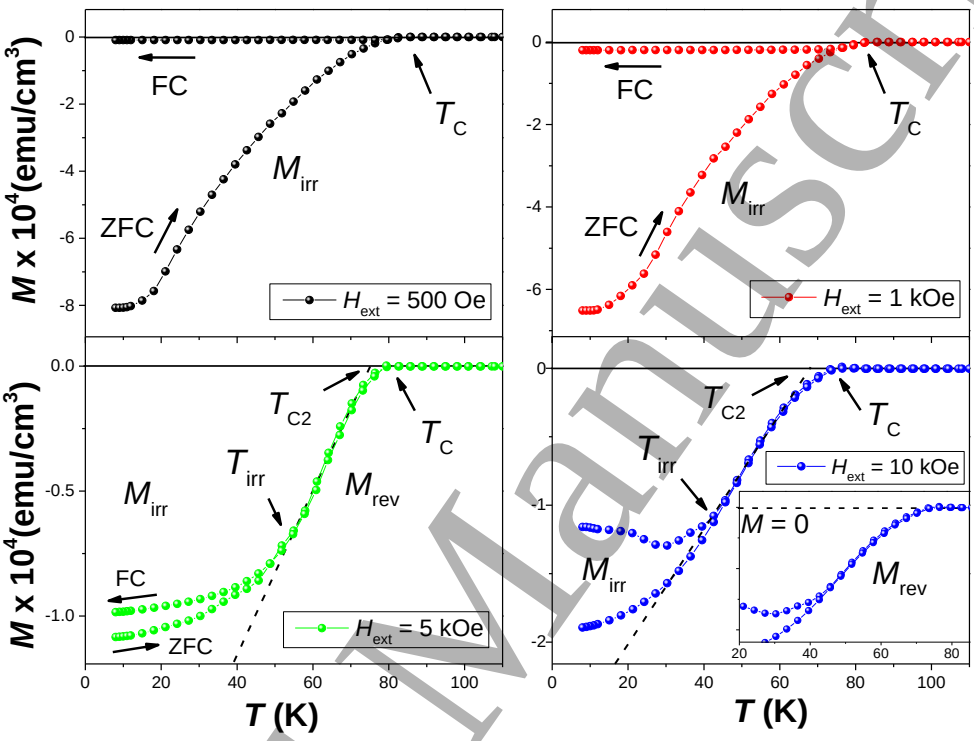

Fig 2. $M(T)$ curves measured at H_{ext} = 500, 1000, 5000 and 10000 Oe. The characteristic temperatures are showed as well as the reversible and irreversible magnetization ranges.

The experimentally-obtained critical field values are summarized in Table 1 and the magnetic phase diagram for the YBCO film is presented in the Fig. 3. The inset figures present a zoom of the $B - T$ diagram near T_c and the critical state crossover.

Table 1. Lower critical field, irreversibility field and upper critical field values estimated from $M(H)$ and $M(T)$ measurements.

Experimental data source	***T* (K)**	H_{C1}**(Oe)**	H_{irr} **(Oe)**	H_{C2} **(Oe)**
Hysteresis loops	10.00	703.41	69948.54	121064.15
	20.00	402.28	51424.23	107106.18
	30.00	301.69	50072.57	105347.51
	40.00	100.73	32626.29	82104.71
	50.00	90.14	27612.95	64326.24
	60.00	50.00	15073.53	50075.92
	70.00	30.00	12564.99	32795.68
***M*(*T*)**	79.81	-	3592.66	10000.00
	82.62		2080.48	5000.00

	85.57		740.35	1000.00
	85.70		689.28	500.00

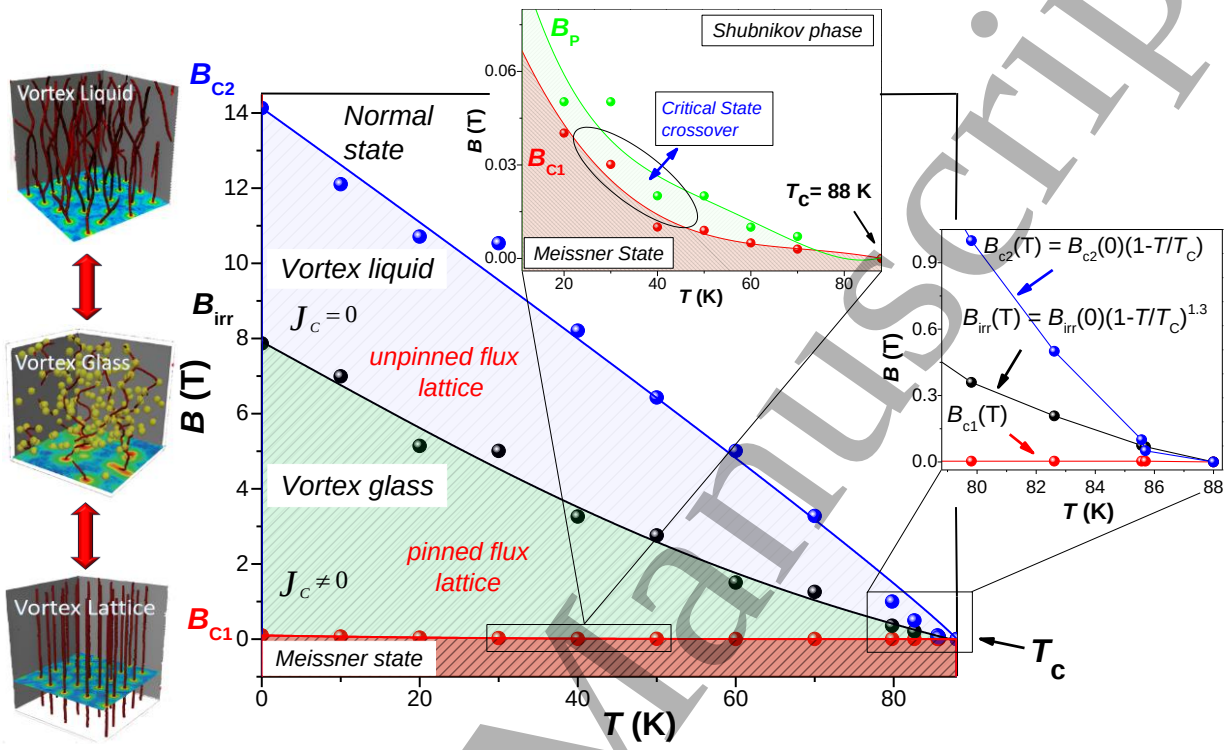

Fig 3. Vortex phase diagram for a uniaxial YBCO textured film. The critical magnetic field values were obtained from several hysteresis loops and temperature dependence measurements, by differentiating the M_{irr} and M_{rev} signals. The upper inset plot shows the transition between the Meissner and the vortex state in more detail, including the region $B_{C1} < B < B_P$ where is not possible to apply the critical state model. The right inset plot shows the data nearby T_c. The schematic representation in the left side (taken from reference [31] with permission from the IOP publishing) shows the vortex lattice for each state.

3.2.- *Critical current density*

Figure 4(a) shows the $J_C(H)$ isothermal curves obtained with the critical state Bean model. In contrast to the loop taken at 10 K, an abrupt decrease on the J_C values are observed at 20 - 30 K. This is caused by the disorder of the CuO_2 superconducting planes along the *ab*-plane, which prevents the transport without loss of energy when increasing the temperature. This was expected since the sample consisted of a uniaxially textured film as confirmed by the XRD (see Fig. S3). Previous works show a strong relationship between the YBCO crystallites order and the J_C improvement, in which lower values than 10^6A/cm^2 are typical for uniaxial texture, while higher values are reported for well-ordered biaxially textured films (both at 77 K, self-field) [20]. A comparison of several $J_C(H,T)$ values with different textured YBCO films grown onto MgO has been previously reported elsewhere [5]. Considering the anisotropy and the uniaxial texture of the YBCO film in the present work, a clear drop in the J_C values is also obtained for applied magnetic fields stronger than 1 T. In addition, the weak peak effect noted at different temperatures (see inset Fig. 4(a)), is confirmed by its influence in vortex regimes transitions, as explained in more detail in the next section. The

peak effect indicates twin structures, intrinsic pinning of vortices at the CuO_2 planes, secondary phase particles, or clusters of oxygen vacancies [19, 32].

The temperature-dependence of the critical current density, $J_C(T)$, is shown in the Fig. 4(b). The experimental data were fitted with the equation 5, which is the typical exponential decay of the J_C [33] and shown as solid lines in the figure. The estimated $J_0(\mu_0 H)$ values are listed in Table 2. Extrapolating the semi-logarithmic data (presented in the inset figure), the value J_C (at $\mu_0 H = 0$ T, 77 K) $\sim 10^5 A/cm^2$ is estimated. Higher magnetic field values imply a rapid transition to flux creep in the sample, as shown in the inset figure, where the experimental deviation from the linear power-law is noted.

$$J_C = J_0 \exp\left(-\frac{T}{T_0}\right) \tag{5}$$

Table 2. J_0 values at different applied magnetic field. The data were obtained from the figure 4.

$\mu_0 H$	0.5 T	1 T	2 T	3 T	4 T
J_0	3.73×10^8	4.30×10^8	3.82×10^8	7.67×10^7	4.83×10^7

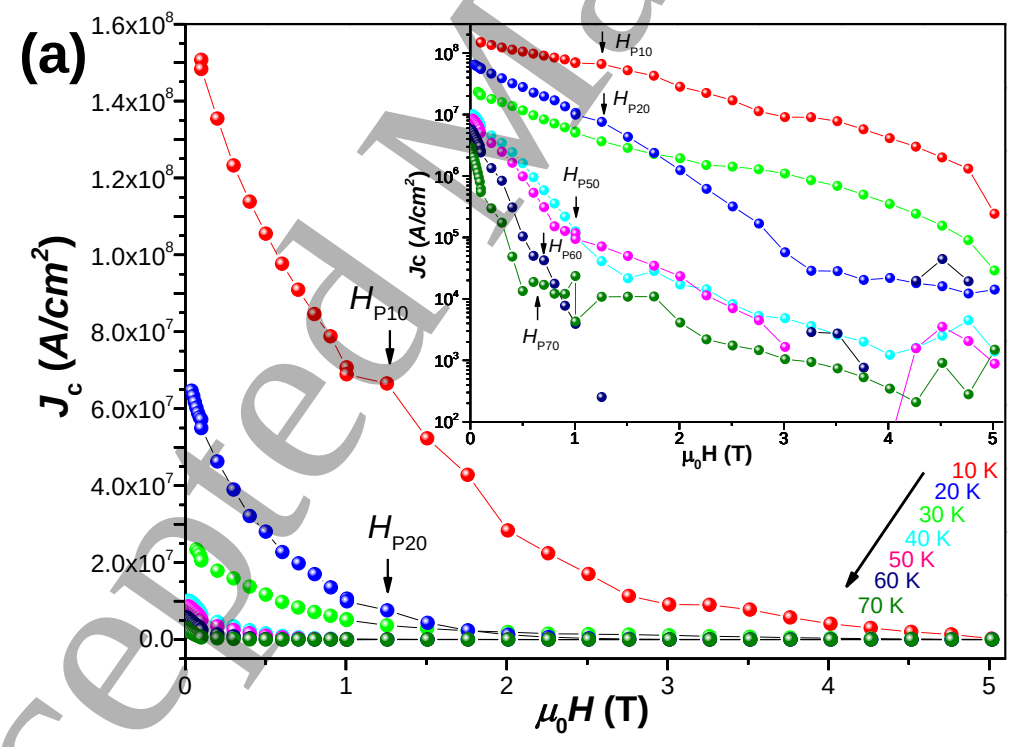

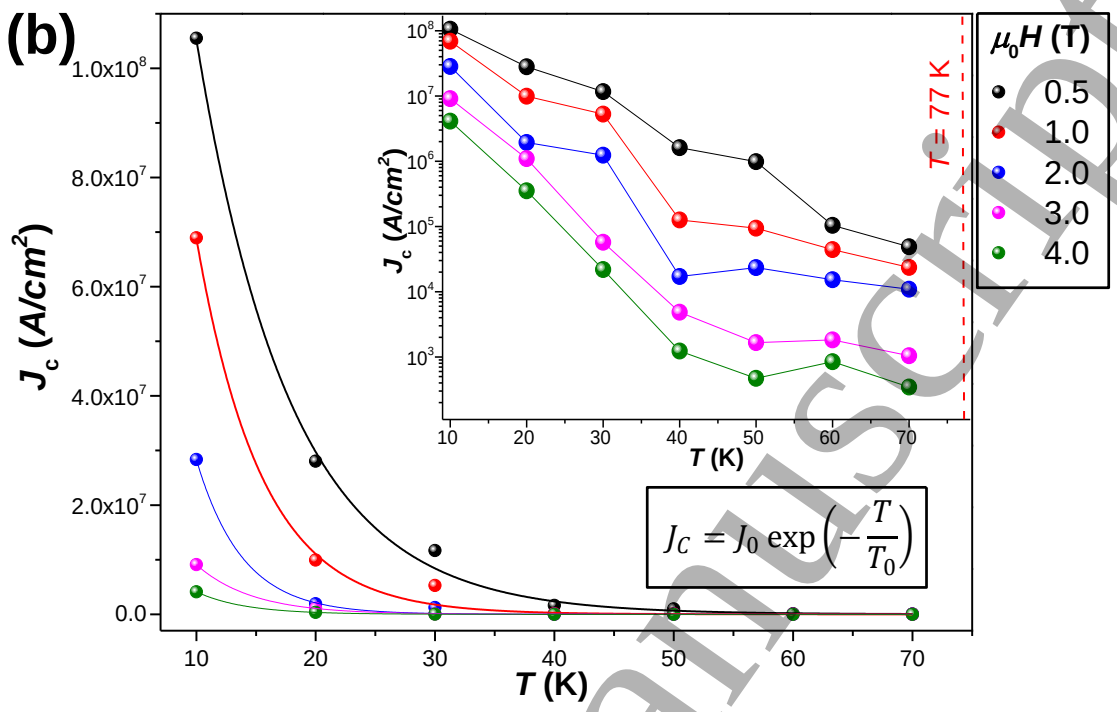

Fig 4. a) Critical current density values at different temperatures. The peak effect is apparently noted at 10 and 20 K. Inset: semi-logarithmic plot where the effect peak is apparently observed at different temperatures. b) $J_C(T)$ data at several applied magnetic fields obtained by the Bean model. The data were fitted with Eq. (5) in order to estimate the $J_0(T)$ values. Inset: semi-logarithmical $J_C(T)$ curves, where experimental deviation from the linear power-law is noted.

3.3.- *Vortex dynamics*

The Ovchinnikov and Ivlev [18] formulation was applied in the $J_C(H,T)$ data to study the vortex dynamics in the uniaxially textured YBCO film. This formalism considers a large number of pinning sites spread over the film. The theory starts statistically averaging the pinning forces of the different defects as in weak collective pinning, but evaluating the probability that a vortex line eventually encounters a pinning site. Note that, in the present work, the YBCO film is not doped and thus, no artificial pinning centres should be considered. In contrast, the vortex pinning mechanism in the film corresponds to intrinsic pinning sites acting as spread pinning sites, in agreement to the development.

The theory was applied by Van der Beek *et al* [19] to analyse YBCO films deposited by pulsed laser deposition on single-crystal substrates assuming sparse strong pinning centres [19]. By extending the theory, the power-law region of $J_C(B)$ is described by two functions with a crossover around an "accommodation field" (B_a). With these assumptions, the following $J_C(B)$ relationships were obtained for various regimes of the magnetic flux density B, for the field $H_{ext} \parallel c$-axis [34]:

$$J_C \approx 0.28 n_i^{\frac{1}{2}} J_0 \frac{[D_i^z F(T)]^{\frac{3}{2}}}{2\varepsilon} \qquad \text{for} \quad B < B^* \qquad (6)$$

$$J_C \approx 0.0866 n_i J_0 \frac{[D_i^z F(T)]^{\frac{9}{4}}}{\varepsilon^{5/4} \xi^{1/2}} \left(\frac{\Phi_0}{B}\right)^{5/8} \qquad \text{for} \quad B^* \ll B \ll B_a \qquad (7)$$

$$J_C \approx 0.375 n_i J_0 D_i^z F(T) \frac{\Phi_0}{B} \qquad \text{for} \quad B \gg B_a \tag{8}$$

Here, n_i is the defect density, $J_0 = (\frac{B_C}{3\sqrt{6}\pi\lambda})(\frac{4\pi}{\mu_0})$ [34] is the depairing current density, ε is the anisotropy parameter ($\varepsilon \approx \frac{1}{5}$ for YBCO [35]), ξ is the in-plane coherence length, D_i^z is the extent of the defects along the field direction, and D_i is their transverse extent (perpendicular to the field direction) [18]. Also, $F(T) = ln\left[1 + D_i^2/2\xi^2(T)\right]$ [34] is a temperature-dependent factor and depends of the coherence length $\xi(T)$. From force-balance considerations, is approximately $F(T) \approx (\frac{4}{D_i^z})(\frac{U_p}{\varepsilon_0})$ [34]. Also, U_p and Φ_0 are the pinning energy per defect and the flux quantum, respectively.

For the OI model, D corresponds to the characteristic length scale over which a defect influences the superconducting properties, such as vortex pinning. It represents the physical dimension of the defect where its perturbing effects on the superconductivity are observable [18, 19].

In order to apply the theorical development to the present work, J_C is plotted in a log-log scale (see Fig. 5(a)). Four different regions are noted in the plot and they are separate by dash lines to eye-guide. In the first region (so-called Regime I), the strength magnetic field is low and each single-vortex is individually pinned. The vortices do not interact and $J_C(\approx$ constant) follows the relationship described in Equation (6). The low magnetic field also generates low density of flux lines in the film. The lines penetrating the sample, or vortex, are randomly distributed in the material with low density with respect to the bulk. Eventually, this regime ends at the so-called accommodation field B^*. $B^*(T)$ corresponds to the characteristic field from which the density of vortices exceeds the pinning sites ones and vortex-vortex interaction takes place. There are two considerations during the estimation of the pinning sizes in Regime I: i) The temperature-dependent factor $F(T) \approx 1$ for isothermal curves (i.e. neglecting the experimental thermal fluctuations contribution) [36] and ii) The geometry of the pinning centres is spherical $D_i^z \approx D$ [34]. Thus, Equation (6) becomes:

$$\frac{J_C}{J_0} = 0.14 \frac{{n_i}^{1/2} D^{3/2}}{\varepsilon} \quad \Rightarrow \quad n_i D = (\frac{J_C}{J_0})^2 \frac{1}{0.49 D^2} \tag{9}$$

As mentioned above, B^* is the boundary field for Regimes I and II from which J_C becomes field dependent, i.e. the point where the vortex-vortex interaction becomes relevant in the system. It is expressed as $B^* \equiv \pi\Phi_0 n_i (U_P/\varepsilon_0)$ [34], where $U_P \approx \varepsilon_0 D F(T)/4$ is the pinning energy per defect and ε_0 is the vortex energy scale. Then, the accommodation field can be expressed as $B^* \approx \pi\Phi_0 n_i D/4$, and after combining with Equation (9), it is obtained:

$$B^* \approx \frac{\pi\Phi_0}{4\text{x}0.49 D^2}\left(\frac{J_C}{J_0}\right)^2 \quad \Rightarrow \quad D \approx \sqrt{\frac{\pi\Phi_0}{1.96 B^*}}\left(\frac{J_C}{J_0}\right) \tag{10}$$

By using the experimental values for J_0 and taking the accommodation field value $B^* = 0.200748$ T from Fig. 5(a) (at 10 K), the pinning centre size in the present work can be estimated by using Equation (10). Thus, $D_{\text{I–II}} \approx 52.31$ nm. On the same way, from the relation $B^* \approx \pi\Phi_0 n_i D/4$, the defect density $n_i \approx 2.33 \text{ x } 10^{21}$ m^{-3} is obtained. This defect density value is in agreement with previous works, where sparse insulating or normal metallic second-phase inclusions are reported [23, 24].

All irregularities disrupting the translational symmetry in a superconductor can pin vortices. The relatively large size $D_{\mathrm{I-II}}$ found with respect to the coherence length reflects the three-dimensionality pinning mechanism for this regime. Whereas 3D pinning sites are characterized by sizes largely exceeding the superconducting coherence length [31, 37, 38] and they usually correspond to spherical or nonuniform secondary phases [21]. Note that the studied film in the present work is not doped, however secondary phases spontaneously form during the YBCO film growth [29, 36]. In fact, the XRD analysis above reveals the presence of secondary phases such as Y_2BaCuO_5 (Y211), which should act as pinning sites. This is in agreement with similar works reported by other authors [39-42], in which the green phase is reported to work well for pinning vortex.

As the magnetic field intensity increases ($B > B^*$), J_C falls following a power-law field dependence $J_C \propto H^{-\alpha}$, as shown in Fig. 5(a) for all the experimental temperatures. The behaviour corresponds to a second regime (Regime II) which is characterized by a large flux lines density and a not negligible vortex-vortex interaction. Van der Beek predicted a power-law $J_C = C(T)H^{-\alpha}$ with $\alpha = \frac{5}{8} = 0.625$ as described in Equation (7), where the exponent α depends on the pinning mechanism [19]. The pre-factors $C(T)$ and exponent α values obtained by fitting the data are listed in the Table 3. The crossover field B^* between Regimes I-II is employed for the estimation of $D_{\mathrm{I-II}}$. Following the Ovchinnikov - Ivlev (OI) model, the Y211 pinning sites mechanism also applies for Regime II.

When the magnetic field reaches the crossover field B_{a}, another power-law region is expected in agreement to the Ovchinnikov - Ivlev approach and following equation 8 (Regime III). However, depending on the composition of the superconductor sample, there are cases in which the magnetic field dependence of J_C [33,43-45] do not reveal Regime III. Nevertheless, in the present work, Fig. 5(a) confirms its presence. Besides, the crossover field B_a between the expression (7) and (8) correspond to the characteristic field $B_a = \Phi_0(\varepsilon\frac{\varepsilon_0}{U_P})^2$. In this way, the expression for the pinning energy per defect is $U_P \approx \varepsilon_0 DF(T)/4$, and taking the same considerations as for Regime I, the following expression is obtained:

$$D \approx \frac{4\varepsilon}{\sqrt{B_a/\Phi_0}} \tag{11}$$

Where the pinning centre size $D_{\mathrm{III}} \approx 30$ nm is found by using the crossover field B_a =1.48 T (at 10 K, Fig. 5(a)) in Eq. (11). Despite the difference between D_{III} and $D_{\mathrm{I-II}}$ above, the Y221 phase still fulfils the pinning mechanism assumption taking into account that the experimental B^* is usually affected by seld-field effects [36]. Therefore, the decay of J_C in comparison to Regime II is caused by the intensity of the vortex-vortex interaction.

Table 3 summarizes the exponent and pre-factor values found by fitting the $J_C = C(T)H^{-\alpha}$ expression for Regime III. As noted from Equation (9), the OI model predicts $\alpha = 1$ for this regime. In contrast, the α values in this work exceed the unit and the J_C values decay more rapidly. This behaviour is caused by the faster relaxation at high magnetic fields, where the measured J_C is much lower than the real critical current density, leading to the apparent steeping of the slope in the double-logarithmic $J_C(B)$ curves. The magnetic relaxation is discussed in detail in the next section.

Table 3. The pre-factor values $C(T)$ and exponent α values from the power-law $J_C = C(T)H^{-\alpha}$ for a uniaxially textured YBCO film grown onto a MgO substrate. The fitted data corresponds to the regime II and III from figure 5(a).

Regime		10 K	20 K	30 K	40 K	50 K	60 K	70 K
II	α	0.483	0.949	0.698	0.650	0.706	0.869	1.076
	$C(T)$	5.0115	1.41×10^{16}	9.807×10^{9}	6×10^{8}	6.921×10^{8}	1.027×10^{9}	1.19×10^{9}
III	α	2.298	1.465	2.280	3.247	3.458	4.686	4.567
	$C(T)$	2.18×10^{17}	3.80×10^{12}	1.41×10^{16}	1.7×10^{18}	6.18×10^{18}	2.369×10^{22}	1.34×10^{21}

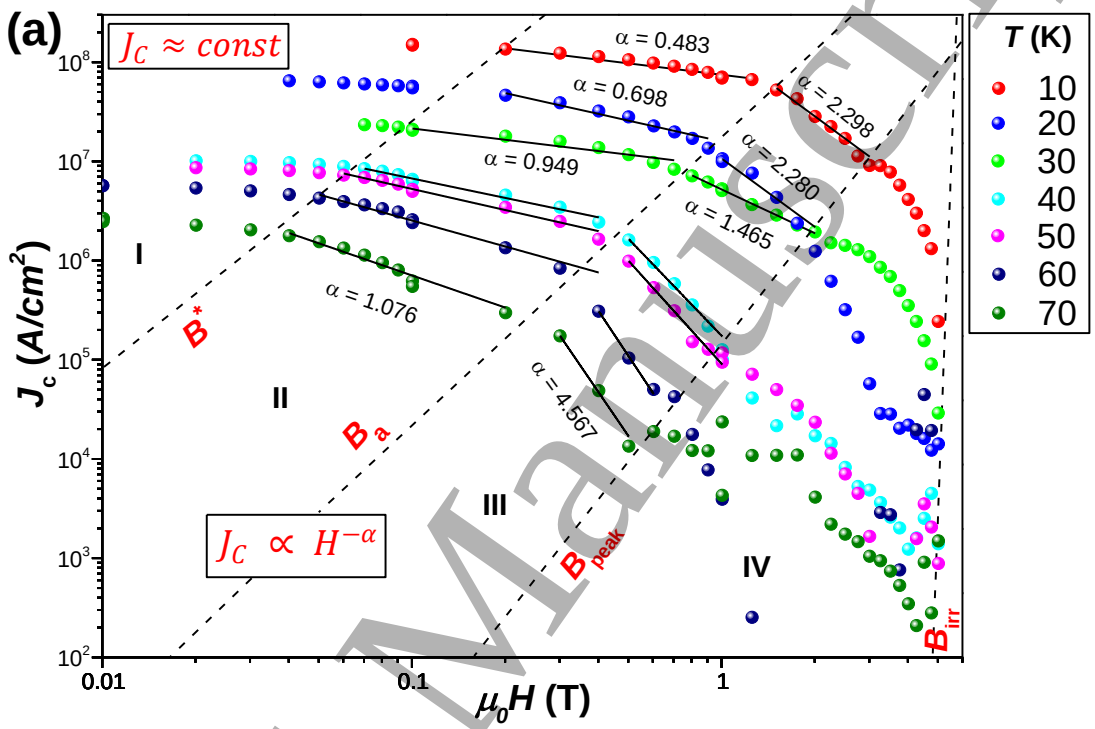

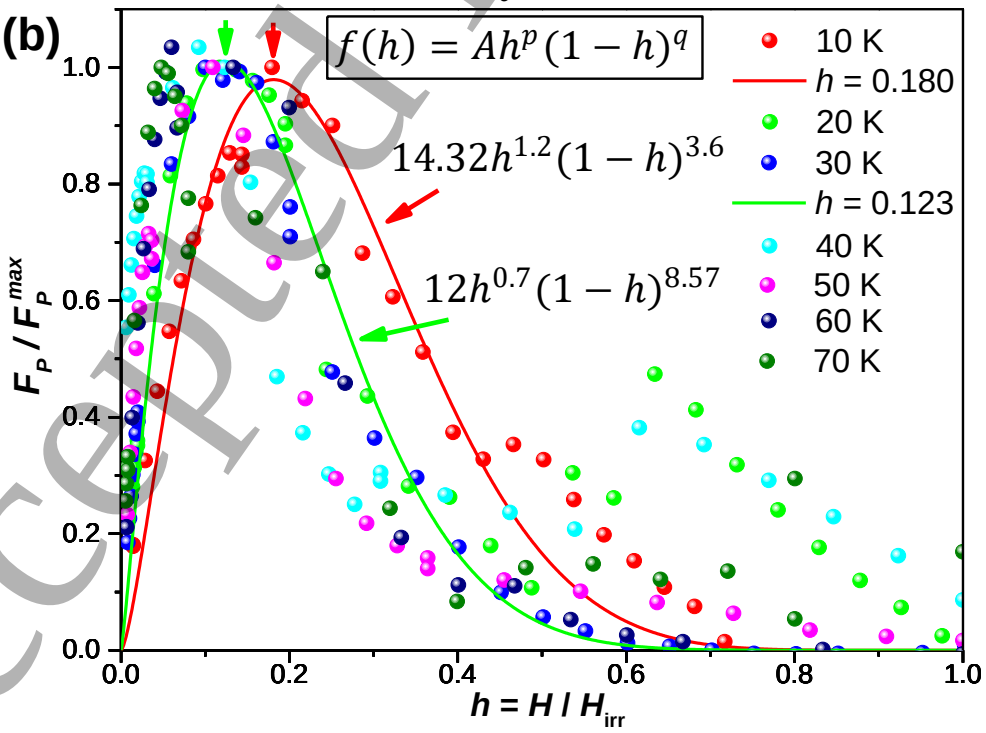

Fig. 5. a) Double-logarithmic plots of the field dependence of J_C at T = 10 – 70 K for a uniaxially textured YBCO film grown onto a MgO substrate. The four regimes discussed in the text are clearly visible and the crossover fields are noted as dotted lines. The solid lines are fits to the power-law $J_C = C(T)H^{-\alpha}$. b) Normalized pinning force $f(h)$ versus normalized magnetic field h at different temperatures.

The well-known secondary peak effect is detected at different temperatures in Fig. 4(a) above. The $B_{\text{peak}}(T)$ values are listed in Table 4 and they correspond to the crossover line between the Regime III-IV, as shown in Fig 5(a). The presence of the secondary peak effect is proved since the experimental B_{peak} values are fitted with the expression $B_{\text{peak}} \propto \left[1 - (\frac{T}{T_C})^4\right]^n$ (see Fig. S2(c)) and they are in agreement with the values reported for YBCO [46, 47]. Finally, the experimental B_{peak} values at each temperature were plotted as a single dotted line in Fig. 5(a). From the figure, it is noted that J_C decreases abruptly to zero in the Regime IV zone.

The field dependence of the pinning force is analysed to find a possible change in the pinning mechanism at different T in the Regime IV zone. The pinning force $F_{\text{P}}(H,T)$ was calculated from the temperature dependence of the J_C curves shown in Fig. 4 above following the expression $F_{\text{P}} = J_C \mu_0 H_{ext}$. The $F_{\text{P}}(H,T)$ curves are shown in Fig. S4, while the estimated $F_P^{max}(T)$ values for each temperature are plotted in Fig. S2(d) using the Kramer scaling law [20, 48]:

$$F_{\text{P}} = [B_{irr}(T)]^m f(h) \tag{12}$$

where $f(h) = F_{\text{P}}/F_P^{max}$ is the normalized pinning force and $h = H/H_{irr}$ is the reduced field. From the double-logarithmical plot, the exponent m = 2.12 is found. Considering this, the pinning force can be expressed as $F_{\text{P}} = [B_{irr}(T)]^{2.12} f(h)$. If the same pinning mechanism dominates over a certain temperature range, then, $F_{\text{P}}(H,T)$ can be scaled as [20]:

$$f(h) = Ah^p(1-h)^q \tag{13}$$

where A is a constant, while p and q are exponents that depend on the pinning mechanism. This scaling law expression is useful in practical cases for estimation of the pinning characteristics under difficult circumstances for experiments.

Figure 5(b) shows the $F_{\text{P}}/F_P^{max}(h)$ dependence at different temperatures. A clear change in the pinning mechanism is observed at 10 K, as evidenced by a shift in the field at the maximum F_{P}. The change in the pinning mechanism at low temperatures can be attributed to the contribution of intrinsic defects in the pinning process at this temperature range.

With the aim to corroborate that the change in the pinning mechanism has not relation of the kind of pinning centres, the pinning centre size is estimated at $B = B_{\text{peak}}$. According to the OI approach, Regime IV is governed by Equation (8); and taking the previous considerations $F(T) \approx 1$ and $D_i^z \approx D$, the pinning center size at 10 K is D_{IV} = 40 nm, which is in agreement to the D_{I-II} and D_{III} values found above.

From Equation (13) and Fig. 5(b), the pinning for the system can be expressed as $F_{\text{P}} = 12[B_{irr}(T)]^{2.12} h^{0.7}(1-h)^{8.57}$, which is valid for the temperature range 20 – 70 K. On the other hand, F_{P} at low temperatures range as $F_{\text{P}} = 14.32[B_{irr}(T)]^{2.12} h^{1.2}(1-h)^{3.6}$.

Table 4. $B_{\text{peak}}(T)$ values experimentally obtained and calculated from Fig. S2(c).

	B_{peak10}	B_{peak20}	B_{peak30}	B_{peak40}	B_{peak50}	B_{peak60}	B_{peak70}
Experimental (T)	1.25	Not found	1.26	Not found	1.01	0.70	0.60
Calculated (T)	1.25	1.24	1.22	1.16	1.05	0.81	0.51

3.4.- *Magnetic relaxation*

The magnetic relaxation was measured at different temperatures in order to determine the relationship between the current density and the effective activation energy (see Fig. S5). The $M\ vs\ \ln t$ curves presented in the inset plot in Fig. S5 do not decay linearly, but the slow decrease in the relaxation rate is a general property for HTSC [16]. Taking this into account, the current dependence of the effective activation energy $U_{eff}(J)$ is non-linear and the magnetic relaxation cannot be explained in the framework of the thermally activated flux-creep theory proposed by Kim-Anderson [13]. In this case, the nonlinear behaviour has been inspected by many theorical efforts, specifically by vortex-glass and collective pinning theories. Note that the logarithmical barrier model proposed by Zeldov [15] does not include the crucial μ exponent which gives information about the presence of different vortex regimes. Thus, it is discarded in the present work. These valid models give a similar inverse power law type barrier [49, 50]:

$$U_{eff}(J,T,B) = \frac{U_0(T,B)}{\mu}\left[\left(\frac{J_{C0}}{J}\right)^{\mu} - 1\right] \tag{14}$$

where $U_0(T,B)$ is the characteristic pinning energy, J is the current density that is far below J_C, J_{C0} is the critical current density at which the barrier vanishes and μ is the glassy exponent which determines the nature of the pinning barrier. The μ exponent gives information about the size of the vortex bundle and it allows to differentiate between the Kim-Anderson ($\mu = -1$), vortex-glass ($\mu \leq 1$) and collective pinning (different values as 1/7, 7/9 and 3/2, depending of the collective pinning regime) [20] models. Considering that all the relaxation curves were measured at the same magnetic field $\mu_0 H = 1$ T, then $U_{eff}(J,T,B) = U_{eff}(J,T)$.

The thermal function $G(T)$ is defined as $U_0(T,B) = U_0(B)G(T)$ and thus, $U_0(B) = U_0$. The thermal function accounts for various temperature dependences and serves to establish a continuity of $U_{eff}(J)$ under conditions of lower density current and elevated temperatures.

With the aim to obtain experimentally U_{eff} and therefore determine the nature of the flux creep, Maley *et al* [51] developed a useful analysis to calculate the pinning energy based on a relaxation time approximation:

$$U_{eff} = -Tln\left|\frac{dM}{dt}\right| + TA \tag{15}$$

where the relationship between M and J_C is given by the Bean model, previously described in Equation (4). $A = \ln(J_C/\tau)$ is a time independent constant, related to the average hopping velocity and τ is an unknown macroscopic attempt time for vortex hopping. The method proceeds by plotting the experimental data using Equation 15 and adjusting the A constant to produce a smooth curve of $U_{eff}(T,J)$ at low temperatures, as shown in the inset figure in Fig. 6(a), where the experimental value $A = 52$ is obtained. A correct estimation of A warranties that the fundamental superconducting parameters, penetration depth and coherence length

does not vary much. The Maley method takes in account the rapid magnetization decay rates usually observed for HTSC materials [51].

The Maley model typically provides an estimate of the average pinning energy per vortex rather than the sum of pinning energies of all vortices within the film. Therefore, the pinning energy obtained from the Maley model represents the average energy required to pin a single vortex due to the collective effect of defects or impurities. It does not directly sum up the energies of all vortices present in the film.

The thermal function $G(T)$ was used to approximate the temperature dependence of U_{eff}. As mentioned above, considering $U_{eff}(T,B) = U_{eff}G(T)$, it is possible to obtain $U_{eff} = U_{eff}(T,B)/\ G(T)$. By applying this thermal function in the inset figure in Fig. 6(a), the continuity of the pinning energy at low J and at high temperatures is warranted, as it is observed at 60 K. The following empirical thermal function was used in the present work [20, 52]:

$$G(T) = \left[1 - (\frac{T}{T_C})^2\right]^{3/2} \tag{16}$$

The J dependence of the U_{eff} is shown in Fig. 6(a), where the data is plotted and fitted using the Equation (14). The glassy obtained exponent μ = 0.87 matches well with the vortex-glass model. However, the data obtained at 30 K does not exactly fall on the fitted curve, which might be caused by thermal fluctuations during performing the measurement or the used pinning energy model is not suitable for this case.

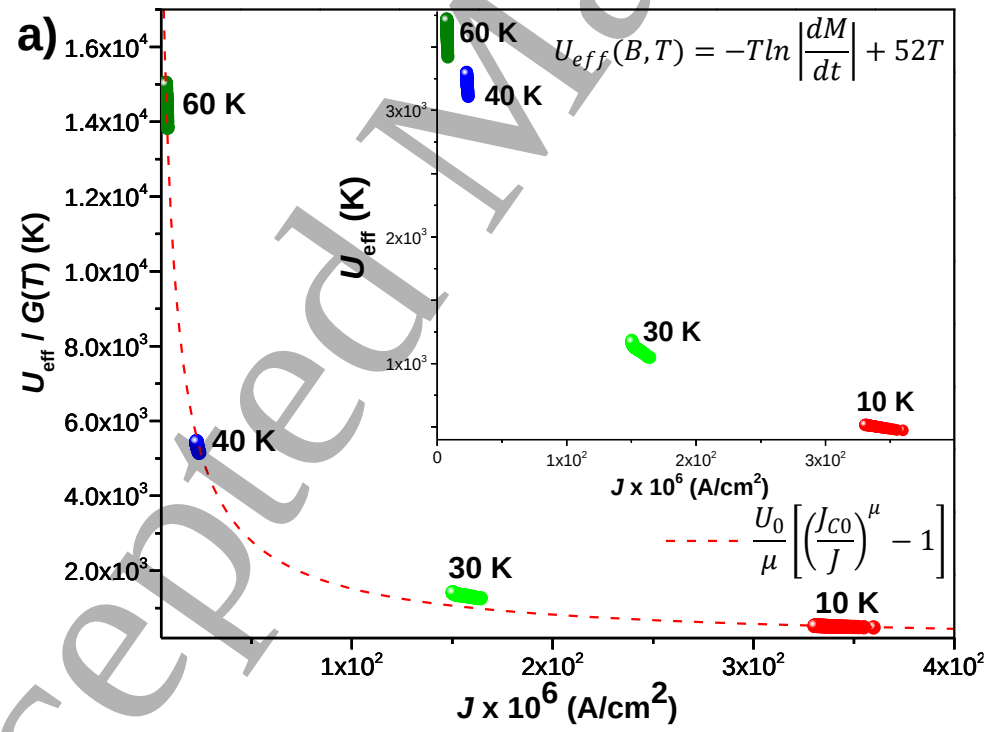

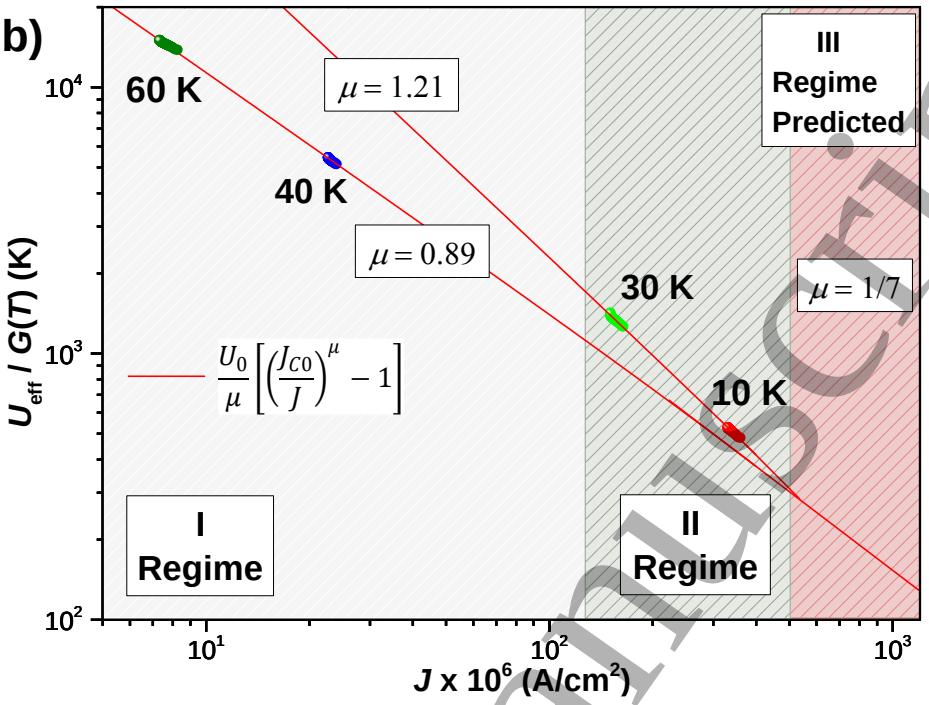

Fig 6. a) $U_{eff}(J)$ curves obtained by apply the Maley method. The fitted dotted curve corresponds to the vortex-glass model equation. **Inset**: The effective pinning energy $U_{eff}(J,T)$ versus J isothermal curves. b) Experimental results analysis using the collective-pinning model. The analysis allows to observe the existence of different behaviour regime of pinning in the sample.

In order to inspect the J dependence of $U_{eff}(J)$ more closely, the data was plotted on a double-logarithmic scale, as it is shown in Fig. 6(b). Considering the nonlinear behaviour of the data at 30 K, the solid curves show the fitting using Equation (14), were different glassy exponent μ values, 1.21 and 0.89, are obtained. These values suggest that the experimental results follow the collective-pinning model, where μ varies with the dimensionality and length scales for the vortex lattice, resulting in different regimes of vortex pinning. According to this model, for collective pinning by weak point-like disorder is obtained $\mu = 3/2 \approx 1.21$. This applies for small bundles of pinned flux (at higher H_{ext} and T and lower J). This is in agreement with Fig. 6(b). Also, for pinning of large bundles of flux under high applied fields, high temperature and small J, the glassy exponent is around $\mu = 7/9 \approx 0.89$. Additionally, the collective pinning model predicts a third regime with $\mu = 1/7$ for pinning of individual flux lines at low temperatures. This regime is not observed in Fig. 6(b) due to the measuring experimental conditions used in the present work. Previous works report the presence of a single regime (vortex glass) and different behaviour regimes (collective pinning) in the $U_{eff}(J)$ diagram, and depending on the characteristic of the samples. Table 5 lists the results similar works reported in the literature and compared with the present work.

In the present work, the Y211 secondary phase act as collective pinning centres of vortices in the YBCO film at different regimes. Eventually, by employing the A and J_0 values resulted from the fitting, the macroscopic attempt time τ can be estimated from the equation $A = \ln(J_C/\tau) = 52$, giving $\tau \sim 19\text{x}10^{-6}$ s (i.e. in the microsecond range). This represents the scale hopping time for the jump of a single vortex or bundle vortex in different pinning sites. From the obtained pinning regimes, the pinning energy U_0 is estimated by fitting the loops in Fig 4(b). Here, the U_0 values 2.877 and 1.753 meV were obtained for regimes I and II, respectively.

Table 5. Comparison of different glassy exponent, vortex regimes, thickness and vortex model reported in the literature and this work.

Sample	Characteristics	Thickness	Glassy exponent μ values	Number of regimes reported	Vortex model	Reference
(Gd-Y)-Ba-Cu-O	Thin film	0.7 μm	1.7	3	Vortex Glass	[49]
		1.4 μm	1.75			
		2.8 μm	1.65			
YBCO	Biaxially textured Undoped by RABiTS process	34 nm	0.56 – 0.69	3	Collective Pinning	[34]
		170 nm				
		500 nm				
		1450 nm				
YBCO/STO	Prepared by PLD using a target obtained by citrate-gel method	200 nm	0.6; 1.7	4	Collective Pinning	[33]
YBCO/STO	Prepared by PLD using a commercial target	200 nm	0.6; 2.2	4	Collective Pinning	
$Bi_2Sr_2Ca_2Cu_{3-x}Mo_xO_{10+\delta}$	x = 0.0	Glass samples	0.771	3	Vortex Glass	[53]
	x = 0.5		0.773			
	x = 1.0		0.812			
	x = 1.5		0.797			
YBCO/MgO	Undoped uniaxially textured	1 μm	0.89; 1.21 and 1/7 (predicted)	4	Vortex Glass / Collective Pinning	This work

3.5.- *E-J characteristics*

To complete the discussion about the pinning models, the dependence of electric field E on the current density J is studied. Usually, the $E-J$ curves are directly obtained by transport measurements [49] or indirectly obtained by magnetic measurements using VSM or SQUID magnetometers [12]. In the present work, the $E-J$ characteristics are obtained from a combination of swept field (from $M(H)$ loops) and flux creep (from $M(t)$ loops) measurements. The advantage of the indirectly method is the free-dependence of wire contacts which prevents instrumental errors and allows a facile study of the superconducting properties at low temperatures and high magnetic fields. This is an advantage over conventional transport methods in which typically $E{\sim}1\mu V/cm$ is obtained [12]. Furthermore, the dissipation level tends to be self-limiting, thereby precluding the hazard of overheating or destroying the sample. This is observed in the heating of the contacts, restricting the transport measurements at higher temperature and lower currents. In the present work the study is carried out by using a DC-MPMS-SQUID magnetometer as described in the experimental section.

Figure 7 shows the $E-J$ characteristics under $\mu_0 H = 1$ T and plotted in log-log-scale. The data were obtained from swept field (at T = 10, 20, 30, 40, 50, 60 and 70 K) and flux creep (at T = 10, 30, 40 and 60 K) measurement modes. For the swept field rates, the data were obtained from the variation of the magnetic field H during the $M(H)$ measurements (see Fig. S6), taking the magnetization values at applied magnetic fields near to 1 T, where the variation of B was around $dB/dt = 74.76$ mT/s. The J data were calculated with Equation (4), while the induced field E values on the perimeter of the film were obtained using Equation (17). The obtained values lie on the interval 10^{-5} – 10^{-8} V/cm. On the other hand, the creep data was extracted using the Equation (18) in the relaxation measurements shown in Fig. S5, where d and a are the thickness and width of the film, respectively. From the creep measurements, the E data range 10^{-8} – 10^{-11} V/cm.

Figure 7 shows the linear relation between E and J when plotted in a log-log scale. The relationship behaviour corresponds to the power-law relation $E \propto J^n$, where n is the power-law index. As shown in the figure, n is the slope of the $E(J)$ curves at the log-log scale, which reflect the underlying vortex pinning properties of the sample. The n values generally decrease with temperature and applied magnetic field, becoming small at high T and high H [49]. The power-law behaviour provides evidence of a flux-creep process in the film [54]. The collective flux creep theory predicts that the $E(J)$ curves changes from convex (at high J values) to concave curvature (at low J values) [17, 55]. In the limit, when $J \to 0$, the pinning energy $U(J) \to \infty$, meaning that the $E(J)$ curves become gradually steeper. For the case $U(J) \to \infty$, vortex hopping to neighboring sites becomes impossible. The change of curvature is a very slow process as it is observed at 10 and 30 K for the creep measurements, which is in agreement with the theory.

$$E = \frac{d\varphi/dt}{perimeter} = \frac{1}{perimeter}\frac{d}{dt}(area \times magnetic\ field) = \frac{a}{4}\left(\frac{dB}{dt}\right) \tag{17}$$

$$E(J) = \mu_0 \frac{\pi a \mathrm{d}}{12}\left(\frac{dJ}{dt}\right) \tag{18}$$

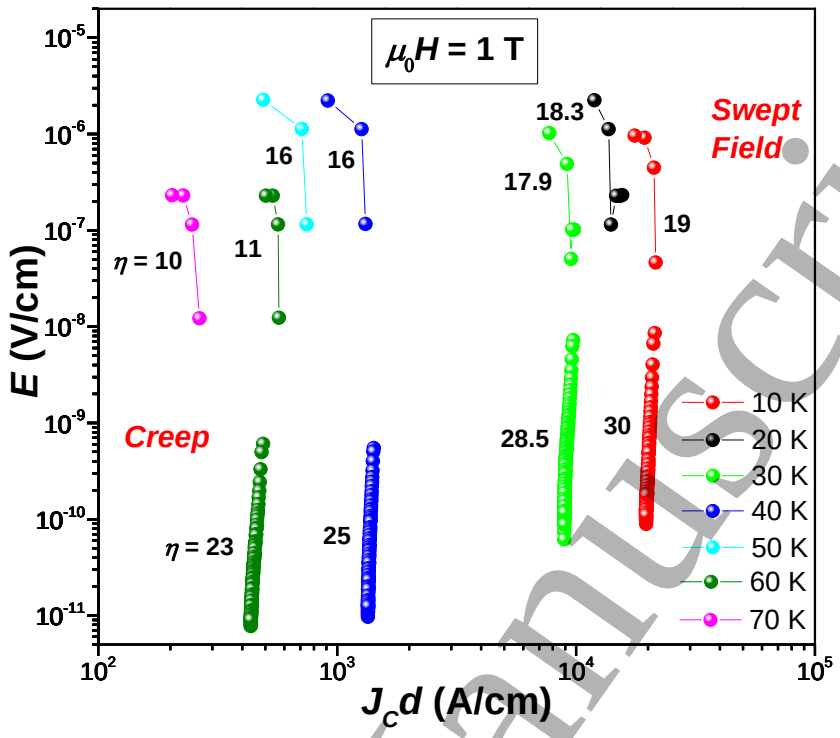

Fig 7. $E(J)$ characteristic curves determined at different temperatures by swept field and creep measurements under an applied magnetic field $\mu_0 H = 1$ T transversal to the YBCO film. The n values were obtained from the power-law $E \propto J^n$.

CONCLUSIONS

The vortex glass and collective-pinning models were applied on the experimentally obtained magnetic data for an undoped uniaxial textured YBCO film and the different obtained regimes were discussed. The presented rigorous analysis of experimental results provides a valuable example on how to apply the theory of vortex dynamics on and YBCO superconducting film. According to the collective-pinning model, a third regime at temperatures lower than 10 K was expected; whereas for the vortex-glass model a single vortex regimen was expected. For both cases, the Y211 secondary phase is found to be the main pinning mechanism in the superconducting system, in agreement with a 3D pinning centre description. According to the field dependence of the pinning force, a change in the pinning mechanism is found at 10 K. This change can be attributed to the contribution of another intrinsic defects with different dimensionality in the pinning process of the system, such as stacking faults, grain boundaries, misoriented grains or point defects.

AKNOWLEDGEMENTS

This work has been supported by the Peruvian Agency of Science CONCYTEC-PROCIENCIA through grant No. PE501085381-2023-PROCIENCIA entitled “Tesis de Pregrado y Posgrado en Ciencia, Tecnología e Innovación Tecnológica - Concurso E073-2023-01”. The work in UK has been supported by the Cambridge Royce facilities grant CAM-YR8-UI-009-REAS. The work in Brazil has been supported by the PROFESSOR VISITANTE Program Nº. 13/2022 of the Universidade Federal de Pernambuco, Brazil, Contract No. 062 /2022 (Process no. 23076.101469/2021-69). A. Aguiar thanks CNPQ, Brazil for supporting his research project.

Authors contribution:

Data acquisition, methodology, data curation and formal analysis (H. Sanchez Cornejo and L. De los Santos Valladares), conceptualization, interpretation, validation, data curation and visualization (H. Sanchez Cornejo, A. Bustamante Dominguez, Ji Won Seo, S.N. Holmes, J. Albino Aguiar, V.A.J. Silva, C.H.W. Barnes and L. De Los Santos Valladares) and all authors have contributed in writing and reviewing the manuscript.

Data availability statement

All data that support the findings of this study are included within the article (and any supplementary files).

REFERENCES

[1] Stangl, A., Palau, A., Deutscher, G. Obradors, X., Puig, T.: Ultra-high critical current densities of superconducting $YBa_2Cu_3O_{7-\delta}$ thin films in the overdoped state. Sci Rep 11, 8176 (2021). https://doi.org/10.1038/s41598-021-87639-4

[2] Sanchez Cornejo, H. *et al*. Texture and terahertz analysis of $YBa_2Cu_3O_7$ grown onto $LaAlO_3$ by the chemical solution deposition technique, Heat Treatment and Surface Engineering, 3:1, 1-8, (2021) https://doi.org/10.1080/25787616.2021.2022294

[3] Bustamante Domínguez, A. *et al*.: Synthesis of $YBa_2Cu_3O_{7-\delta}$ using oxalate precursor and sol-gel method. Advances in Science and Technology Vol. 47 (2006) pp. 37-42. https://doi.org/10.4028/www.scientific.net/AST.47.37

[4] Zhang, C., Du, X., Zhang, H.: Improved biaxial texture of tri-layer YBCO/$CaTiO_3$/YBCO films using an all chemical solution deposition method, Physica C: Superconductivity and its applications 578 (2020) 1353737. https://doi.org/10.1016/j.physc.2020.1353737

[5] Sanchez Cornejo, H., De Los Santos Valladares, L., Barnes, C.H.W., Moreno, N. O., Bustamante Domínguez, A.: Texture and magnetic anisotropy of $YBa_2Cu_3O_{7-x}$ film on MgO substrate. J Mater Sci: Mater Electron 31, 21108–21117 (2020). https://doi.org/10.1007/s10854-020-04623-w

[6] Groves, J.R. *et al*.: High critical current density $YBa_2Cu_3O_{7-d}$ thick films using ion beam assisted deposition MgO bi-axially oriented template layers on nickel-based superalloy substrates, J. Mater. Res., Vol. 16, No. 8, (2001) https://doi.org/10.1557/JMR.2001.0295

[7] Yu, F. *et al*.: Preparation of MgO Self-Epitaxial Films for YBCO High-Temperature Coated Conductors. Micromachines (2023), 14, 1914. https://doi.org/10.3390/mi14101914

[8] Pan, V. M., and A. V. Pan. "Vortex matter in superconductors." Low Temperature Physics 27.9 (2001): 732-746. https://doi.org/10.1063/1.1401182

[9] Gropp, W. D., Kaper, H. G., Leaf, G. K., Levine, D. M., Palumbo, M., Vinokur, V. M.: Numerical Simulation of Vortex Dynamics in Type-II Superconductors, Journal of Computational Physics 123, 254–266 (1996) https://doi.org/10.1006/jcph.1996.0022

[10] Rivasto, E., Huhtinen, H., Hynninen T., Paturi, P.: Vortex dynamics simulation for pinning structure optimization in the applications of high-temperature superconductors, J. Phys.: Condens. Matter 34 (2022) 235902 https://doi.org/10.1088/1361-648X/ac5e78

[11] Sadovskyy, I. A., Koshelev, A. E., Glatz, A., Ortalan, V., Rupich, M. W., Leroux, M.: Simulation of the Vortex Dynamics in a Real Pinning Landscape of $YBa_2Cu_3O_{7-\delta}$ Coated Conductors, Phys. Rev. Applied 5, 014011 (2016) https://doi.org/10.1103/PhysRevApplied.5.014011

[12] Wu, Z., Higashikawa, K., Kiss, T.: Continuous Measurement on Electric-Field Versus Current-Density Characteristics of REBCO Coated Conductors in the Electric-Field Window From 10−2 Down to 10−11 V/m, in IEEE Transactions on Applied Superconductivity, vol. 33, no. 5, pp. 1-5, (2023), Art no. 6601705 https://doi.org/10.1109/TASC.2023.3258375

[13] Kim, Y. B., Hempstead, C. F., Strnad, A. R.: Flux Creep in Hard Superconductors, Phys. Rev. 131, 2486 (1963) https://doi.org/10.1103/PhysRev.131.2486

[14] Yeshurun, Y., Malozemoff, A. P.: Giant Flux Creep and Irreversibility in an Y-Ba-Cu-O Crystal: An Alternative to the Superconducting-Glass Model, Phys. Rev. Lett. 60, 2202 (1988) https://doi.org/10.1103/PhysRevLett.60.2202

[15] Zeldov, E., Amer, N. M., Koren, G., Gupta, A., Gambino, R. J., McElfresh, M. W.: Optical and electrical enhancement of flux creep in $YBa_2Cu_3O_7$ epitaxial films, Phys. Rev. Lett. 62, 3093 (1989) https://doi.org/10.1103/PhysRevLett.62.3093

[16] Ijaduola, A. O. *et al*.: Critical currents, magnetic relaxation and pinning in NdBa2Cu3O7-x films with BaZr03-generated columnar defects, Supercond. Sci. Technol. 25 (2012) 045013 (9pp) http://dx.doi.org/10.1088/0953-2048/25/4/045013

[17] Feigel'man, M. V., Geshkenbein, V. B., Larkin, A. I., Vinokur, V. M.: Theory of collective flux creep, Phys. Rev. Lett. 63, 2303 (1989) https://doi.org/10.1103/PhysRevLett.63.2303

[18] Ovchinnikov, Y. N., Ivlev, B. I.: Pinning in layered inhomogeneous superconductors, Phys. Rev. B 43, 8024 (1991) https://doi.org/10.1103/PhysRevB.43.8024

[19] van der Beek, C. J. *et al*.: Strong pinning in high-temperature superconducting films. Phys. Rev. B 66, 024523 (2002). https://doi.org/10.1103/PhysRevB.66.024523

[20] Krabbes, G., Fuchs, G., Wolf-Rudiger Cander, May, H., palka, R.: High temperature superconductor bulk materials. Wiley-VCH Verlag GmbHCo. KGaA, Weinheim 2006, ISBN: 3-527-40383-3 https://doi.org/10.1002/3527608044

[21] Zhang, J.; Wu, H.; Zhao, G.; Han, L.; Zhang, J.: Progress in the Study of Vortex Pinning Centers in High-Temperature Superconducting Films. Nanomaterials 2022, 12, 4000. https://doi.org/10.3390/nano12224000

[22] Vallès, F. *et al*.: Optimizing vortex pinning in $YBa_2Cu_3O_{7-x}$ superconducting films up to high magnetic fields. Commun Mater 3, 45 (2022). https://doi.org/10.1038/s43246-022-00266-y

[23] T. I. Selinder, U. Helmersson, Z. Han, *et al.*, "Yttrium oxide inclusions in YBa2Cu3Ox thin films: Enhanced flux pinning and relation to copper oxide surface particles", Physica C (Amsterdam) **202**, 69 (1992). https://doi.org/10.1016/0921-4534(92)90297-P

[24] A. Catana, R. F. Broom, J. G. Bednorz, J. Mannhart, D. G. Schlom; "Identification of epitaxial Y_2O_3 inclusions in sputtered $YBa_2Cu_3O_7$ films: Impact on film growth". *Appl. Phys. Lett.* 24 February 1992; 60 (8): 1016–1018. https://doi.org/10.1063/1.106507

[25] Kumar, G., Dahiya, M., Khare, N.: Enhancing pinning ability by the addition of potassium niobate nanorods in YBCO superconductor, Phys. Scr. 98 (2023) 115915 https://doi.org/10.1088/1402-4896/acfd63

[26] Cullity, B.D.: Elements of X-ray Diffraction (Addison-Wesley Publishing Company, Inc. USA, 1956), pp.96-102

[27] Langford, J.I., Wilson, A. J. C.: Scherrer after sixty years: a survey and some new results in the determination of crystallite size. J. Appl. Cryst. 11, 102–113 (1978) https://doi.org/10.1107/S0021889878012844

[28] Eley, S., Miura, M., Maiorov, B., Civale, L.: Universal lower limit on vortex creep in superconductors. Nat. Mater. 16, 409–413 (2017) https://doi.org/10.1038/nmat4840

[29] De Los Santos Valladares, L. *et al*.: A fluorine-free oxalate route for the chemical solution deposition of YBa2Cu3O7 films in Superconductors, edited by Alexander Gabovich, ISBN 978-953-51-4163-1. Intech, Chapter 3, 2015, pp 35-53. https://doi.org/10.5772/59359

[30] L. De Los Santos Valladares, A. Bustamante Dominguez, R. Bellido Quispe, W. Flores Santibañez, J. Albino Aguiar, C.H.W. Barnes, Y. Majima, "The irreversibility line and Curie-Weiss temperature of the superconductor LaCaBaCu3-x(BO3)xO7 with x=0.2 and 0.3", Physics Procedia 36 (2012) 254-359. https://doi.org/10.1016/j.phpro.2012.06.244

[31] Wai-Kwong Kwok, Welp, U., Glatz, A., Koshelev, A. E., Kihlstrom, K. J., Crabtree, G. W.: Vortices in high-performance high-temperature superconductors, Rep. Prog. Phys. 79 (2016)116501 http://dx.doi.org/10.1088/0034-4885/79/11/116501

[32] Nishizaki, Terukazu, and Norio Kobayashi. "Vortex-matter phase diagram in YBa2Cu3Oy." Superconductor Science and Technology 13.1 (2000)

[33] Peurla, M., Huhtinen, H., Paturi, P.: Magnetic relaxation and flux pinning in YBCO films prepared by PLD from a nanocrystalline target. Supercond. Sci. Technol. 18 628 (2005). https://doi.org/10.1088/0953-2048/18/5/009

[34] Ijaduola, A. O., Thompson, J. R., Feenstra, R., Christen, D. K., Gapud, A. A., Song, X.: Critical currents of ex situ $YBa_2Cu_3O_7$ thin films on rolling assisted biaxially textured substrates: Thickness, field, and temperature dependencies, Phys. Rev. B 73, 134502 (2006) http://dx.doi.org/10.1103/PhysRevB.73.134502

[35] Blatter, Gianni, and Boris Ivlev. "Quantum melting of the vortex lattice in high-Tc superconductors." Physical review letters 70.17 (1993): 2621. https://doi.org/10.1103/PhysRevLett.70.2621

[36] Haberkorn, N. *et al*.: Effect of doping on structural and superconducting properties in $Ca_{1-x}Na_xFe_2As_2$ single crystals (x = 0.5, 0.6, 0.75). Phys. Rev. B 84, 064533 (2011). https://doi.org/10.1103/PhysRevB.84.064533

[37] Collomb, D.; Zhang, M.; Yuan, W.; Bending, S.J. Imaging of Strong Nanoscale Vortex Pinning in GdBaCuO High-Temperature Superconducting Tapes. Nanomaterials 2021, 11, 1082. https://doi.org/10.3390/nano11051082

[38] Coll, M. *et al*.: Size-controlled spontaneously segregated Ba2YTaO6 nanoparticles in YBa2Cu3O7 nanocomposites obtained by chemical solution deposition. Supercond.Sci.Technol.27(2014)044008 http://dx.doi.org/10.1088/0953-2048/27/4/044008

[39] Varanasi, C., Barnes, P. N., Burke, J., Carpenter, J., Haugan, T. J.: Controlled introduction of flux pinning centers in YBCO films during pulsed-laser deposition. Appl. Phys. Lett. 26 December 2005; 87 (26): 262510. https://doi.org/10.1063/1.2143112

[40] Sumption, M. D., Haugan, T. J., Barnes, P. N., Campbell, T. A., Pierce, N. A., Varanasi, C.: Magnetization creep and decay in YBCO thin films with artificial nanostructure pinning, PHYSICAL REVIEW B 77,094506 2008. http://dx.doi.org/10.1103/PhysRevB.77.094506

[41] Namburi, Shi, Y., Palmer, K. G., Dennis, A. R., Durrell, J. H., Cardwell, D. A.: Control of Y-211 content in bulk YBCO superconductors fabricated by a bufferaided, top seeded infiltration and growth melt process, Supercond. Sci. Technol. 29 (2016) 034007. http://dx.doi.org/10.1088/0953-2048/29/3/034007

[42] Kim, S. I. *et al*. On the through-thickness critical current density of an YBCO film containing a high density of insulating, vortex-pinning nanoprecipitates. Appl. Phys. Lett. 18 June 2007; 90 (25): 252502. https://doi.org/10.1063/1.2749437

[43] Pyon, S. *et al*. Critical Current Density and Vortex Dynamics in Pristine and Irradiated KCa2Fe4As4F2. Materials 2021, 14, 5283. https://doi.org/10.3390/ma14185283

[44] Mandal, P., Rakshit, D., Sk, T.: Insulating nanoparticle induced pinning in YBCO superconductor: crossover from collective to strong pinning regimes. Appl. Phys. A 129, 650 (2023). https://doi.org/10.1007/s00339-023-06930-5

[45] Pham, A.T. *et al*. Unraveling the Scaling Characteristics of Flux Pinning Forces in $Bi_{1.6}Pb_{0.4}Sr_2Ca_{2-x}Na_xCu_3O_{10+\delta}$ Superconductors. J. Electron. Mater. 50, 1444–1451 (2021). https://doi.org/10.1007/s11664-020-08676-9

[46] Abulafia, Y., Shaulov, A., Wolfus, Y., Prozorov, R., Burlachkov, L., Yeshurun, Y.: Plastic Vortex creep in $YBa_2Cu_3O_{7-x}$ Crystals, Phys. Rev. Lett. 77, 8 (1996). https://doi.org/10.1103/PhysRevLett.77.1596

[47] Deligiannis, K., et al. "New features in the vortex phase diagram of YBa 2 Cu 3 O 7− δ." Physical review letters 79.11 (1997): 2121. https://doi.org/10.1103/PhysRevLett.79.2121

[48] Kramer, E. J.: Scaling laws of flux pinning in hard superconductors, J. Appl. Phys. 44, 1360 (1973). https://doi.org/10.1063/1.1662353

[49] Polat, O. *et al*. Thickness dependence of magnetic relaxation and E-J characteristics in superconducting (Gd-Y)-Ba-Cu-O films with strong vortex pinning Phys. Rev. B 84, 024519 (2011) https://doi.org/10.1103/PhysRevB.84.024519

[50] Yang, H., Ren, C., Shan, L., Hai-Hu Wen: Magnetization relaxation and collective vortex pinning in the Fe-based superconductor $SmFeAsO_{0.9}F_{0.1}$, Phys. Rev. B 78, 092504 (2008). https://doi.org/10.1103/PhysRevB.78.092504

[51] Maley, M.P., Willis, J. O., Lessure, H., McHenry, M. E.: Dependence of flux-creep activation energy upon current density in grain-aligned $YBa_2Cu_3O_{7-x}$, Phys. Rev. B 42, 2639(R) (1990). https://doi.org/10.1103/PhysRevB.42.2639

[52] McHenry, M. E. *et al*. Dependence of the flux-creep activation energy on the magnetization current for a $La_{1.86}Sr_{0.14}CuO_4$ single crystal, Phys. Rev. B 44, 7614 (1991) https://doi.org/10.1103/PhysRevB.44.7614

[53] Kizilaslan, O., Kirat, G., Aksan, M. A.: Magnetic relaxation behavior in the Bi2Sr2Ca2Cu3−xMoxO10+δ system fabricated by glass-ceramic technique, Journal of Magnetism and Magnetic Materials 384 (2015) 186-191 https://doi.org/10.1016/j.jmmm.2015.02.045

[54] Chudy, M., Zhong, Z., Eisterer, M., Coombs, T.: n-Values of commercial YBCO tapes before and after irradiation by fast neutrons, Supercond. Sci. Technol. 28 035008 (2015) https://doi.org/10.1088/0953-2048/28/3/035008

[55] Wallin, M., Girvin, S. M.: I-V characteristics of high-temperature superconductors with columnar defects, Phys. Rev. B 47, 14642 (1993) https://doi.org/10.1103/PhysRevB.47.14642